Static Loads Testing of a High Aspect Ratio Tow-Steered Wingbox

Christine V. Jutte[1]
Craig Technologies, Inc., Merritt Island, FL 32953, USA

Carol D. Wieseman[2], Andrew E. Lovejoy[3], Bret K. Stanford[4]
NASA Langley Research Center, Hampton, VA 23681, USA

Static loads testing was performed on a 39-foot, high-aspect-ratio wingbox comprising carbon fiber tow-steered wing skins that were tailored for aircraft fuel efficiency under aeroelastic loads. The test article was designated the Passive Aeroelastic Tailored (PAT) wing. To date, the PAT wing, which has an aspect ratio of 13.5, is the largest wingbox designed and built to employ variably oriented carbon fibers along the span of the wing. During testing, distributed point loads were applied to the wingbox to simulate both -1g and 2.5g maneuver loads. To determine the wingbox's flexural axis location, individual point loads were applied. The global response of the wing (displacement and rotation measurements) showed similar trends compared to the finite element model predictions, though discrepancies of up to 17% were observed when comparing actual values between model and test. It was concluded that the boundary conditions and nonstructural features of the wingbox were the likely cause of the inconsistencies. The local response of the wingbox (strain measurements), which was much less affected by factors unrelated to tow-steering, exhibited good agreement with the model predictions, validating the modelling techniques employed for tow-steered composites.

I. Introduction

Tow-steered composites are unlike conventional composites, which align fibers along straight paths. Instead, Advanced Fiber Placement (AFP) machines have broadened the design space for composites by enabling carbon fibers to be applied along curved paths; this is recognized as carbon fiber tow-steering [1]. Using this technology, the stiffness of a composite structure can now be tailored both locally and globally for improved structural performance [2], such as for stress and buckling response. Furthermore, when considering structures like aircraft wings, tow steering can also improve a vehicle's aeroelastic performance [3-4], particularly when considered in conjunction with an optimized wing jig shape [5]. The majority of research aimed to understand relationships between tow-steering and aeroelastic response of aircraft vehicles has been purely analytical.

This work presents the results of static loads testing of a 39-foot, high-aspect-ratio wingbox comprising carbon fiber tow-steered wing skins. This test article was designed and tested as part of the NASA Advanced Air Transport Technology Project (AATT), which strives to uncover and utilize technologies that promote energy efficiency and environmental compatibility in transport aircraft. Tow-steered fibers allow for reduced structural weight of the wing, which in turn lowers the fuel consumption, as demonstrated in Ref. [5]. The test article's tow-steered wing skins were designed and tailored for aircraft fuel efficiency under aeroelastic loads; thus, the test article was designated the Passive Aeroelastic Tailored (PAT) wing. To date, the PAT wing, which has an aspect ratio of 13.5, is the largest wingbox designed and built to employ variably oriented carbon fibers along the span of the wing. The purpose of the test was to validate the techniques used for modeling tow-steered composites by applying static loads (i.e., non-

[1] Principal Engineer.
[2] Research Engineer, Aeroelasticity Branch, AIAA Associate Fellow
[3] Research Aerospace Engineer, Structural Mechanics and Concepts Branch, AIAA Associate Fellow
[4] Research Engineer, Aeroelasticity Branch, AIAA Associate Fellow

aeroelastic loads) to the test article and to demonstrate the use of tow-steering at a scale large enough to employ AFP fabrication methods similar to those used for full-scale structural fabrication. Testing was performed in September and October 2018 in the Flight Loads Lab of the NASA Armstrong Flight Research Center (AFRC).

The NASA PAT wing effort was led by NASA Langley Research Center (LaRC). Aurora Flight Sciences designed and built the 39-foot test article. Aurora subcontracted the University of Michigan to determine the optimal arrangement of the carbon fiber orientations on a full scale computational model. The University of Michigan (i) developed a high-fidelity multidisciplinary optimization process to account for static aeroelasticity, (ii) applied scaled-manufacturing constraints to the full scale model to ensure the resulting subscale model still met fabrication constraints, and (iii) optimized the fiber orientations to minimize fuel burn at the vehicle level [6] using a similar optimization approach as was used in Ref. [5]. Aurora subsequently scaled the design to 27% to ensure fabrication and testing compatibility, resulting in the 39-foot test article. NASA AFRC developed the test setup and conducted both ground vibration testing [6-8] and static loads testing, where the latter is the focus of this paper.

II. Test Article

Figure 1 shows the design configuration of the PAT wing test article. The wingbox was based on a variant of the NASA Common Research Model [9] and includes two skins, two spars, and 58 ribs. Both the upper and lower skins of the PAT wing were fabricated using tow-steered composites. The spars and ribs were fabricated using conventional composites. Upon inspection of the fabricated components, the tow-steered wing skins were fully acceptable; however, various areas of concern were discovered within the spars and ribs, resulting in local repairs. The majority of the repairs were ignored as they were minor, but the repairs that were more significant were explicitly modeled within the test article finite element model (FEM). The most significant repair was on the leading edge spar, where the outboard 11 feet of the spar was replaced with an aluminum spar section of nearly equivalent sizing and performance as the carbon fiber spar section it replaced.

The material system of the wing skin was 130gsm HTS45 / E-752-LT slit into 0.25 inch wide unidirectional prepreg tape. Figures 2 and 3 show the steered tow paths for the upper skin and lower skin, respectively. The optimizer was given freedom to determine the primary fiber tow path along the wing, which was the tow path used for 62.5% of the plies that were designated as the 0° plies. The orientations of the remaining plies (divided equally at 12.5%, 12.5%, and 12.5%) were constrained to be oriented 45°, -45°, and 90° from the 0° plies, respectively. The optimizer was also given the freedom to vary the thickness of the laminate throughout the skins.

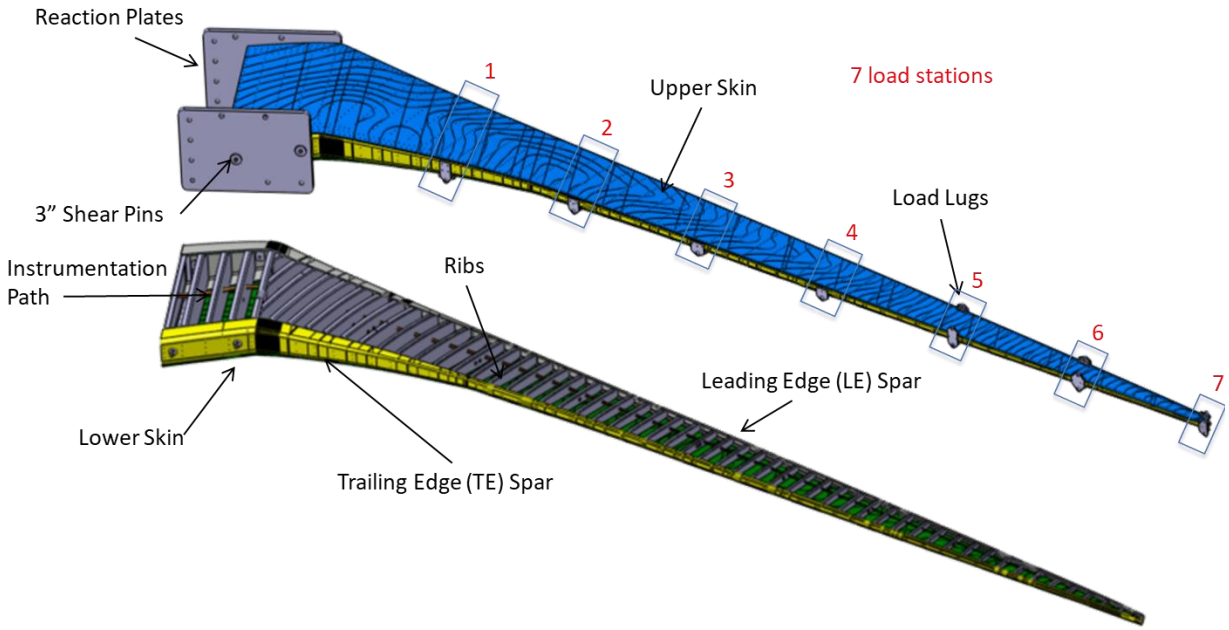

Fig. 1: PAT wing test article. (Solid model provided by Aurora Flight Sciences.)

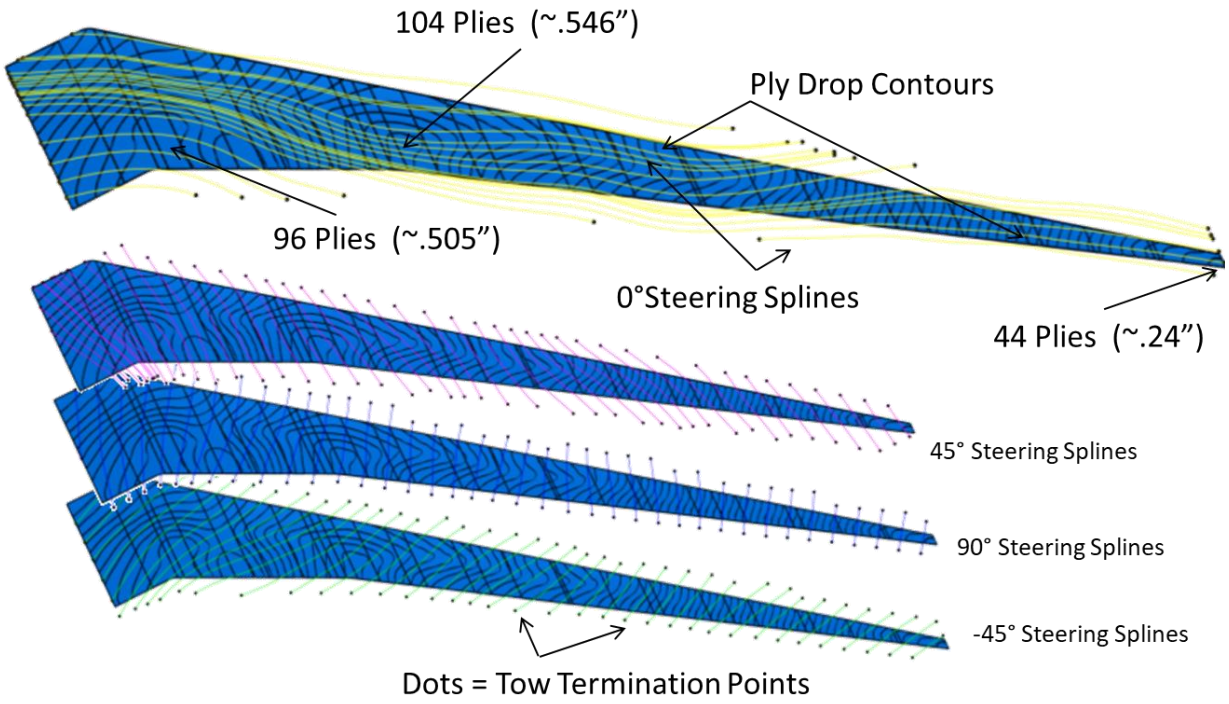

Fig. 2: Tow steering of upper skins. Black lines are the contours of the ply thicknesses. The colored curves are the tow-steering paths. (Graphic provided by Aurora Flight Sciences.)

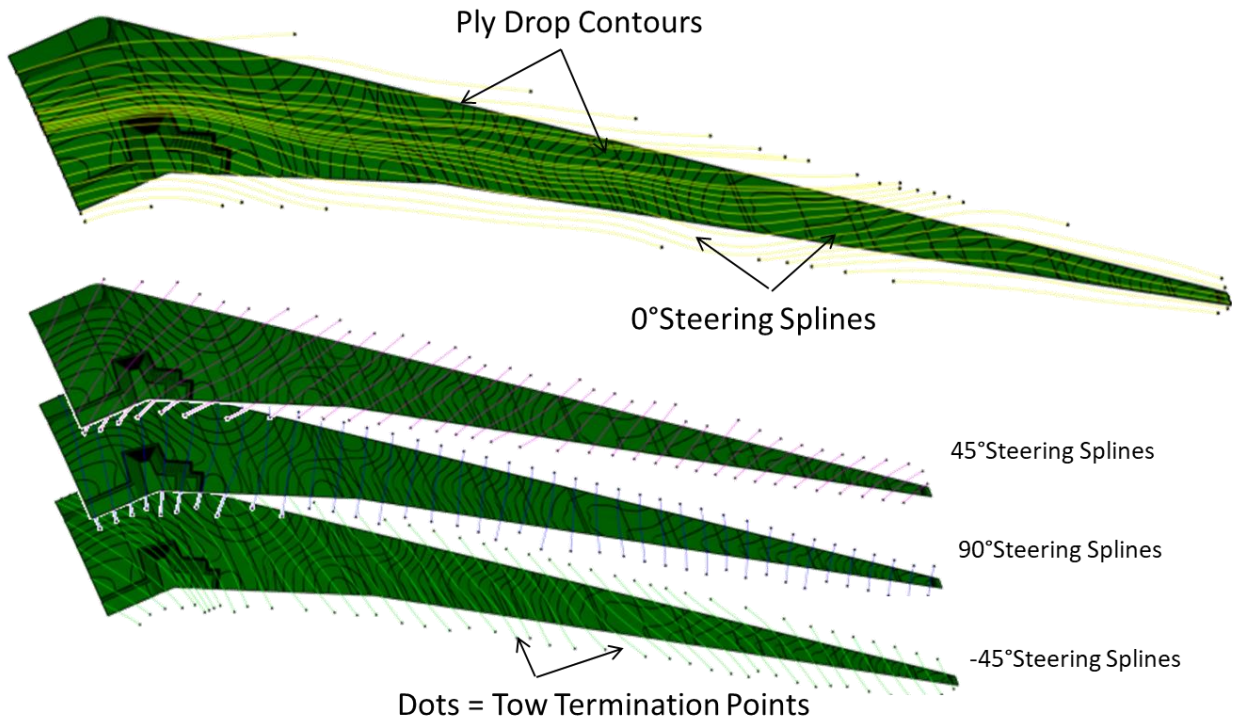

Fig. 3: Tow steering of lower skins. Black lines are the contours of the ply thicknesses. The colored curves are the tow-steering paths. (Graphic provided by Aurora Flight Sciences.)

III. Test Setup

Three types of static loads tests were performed on the wing: -1g maneuver load test, flexural axis test, and 2.5g maneuver load test. Figure 1 shows two reaction plates at the root of the wing. These plates were mounted to AFRC's testing structure. The reaction plates were attached to the spars using four 3-inch pins: two pins on the leading edge (LE) and two pins on the trailing edge (TE). Seven load stations were designated along the length of the wing to simulate distributed aeroelastic loading. Each load station had a pair of load lugs, one mounted on the leading edge and one mounted on the trailing edge. The -1g maneuver test and the flexural axis tests used the same test setup as shown in Fig. 4a, where 14 linear hydraulic actuators were attached vertically between the wing and a ground point below. The third test used a different setup, as shown in Fig. 4b. The four most inboard load stations had linear hydraulic actuators arranged between the wing and a ground point below; however, the actuators were oriented to achieve normal loads (with respect to the deflected wing shape) at the maximum predicted deflection. The three outboard load stations were attached to an overhead loading system comprising three linear actuators connected to pulleys and cables. The cables were attached to the wing and configured to achieve normal loads at the maximum predicted deflection using a whiffle tree approach.

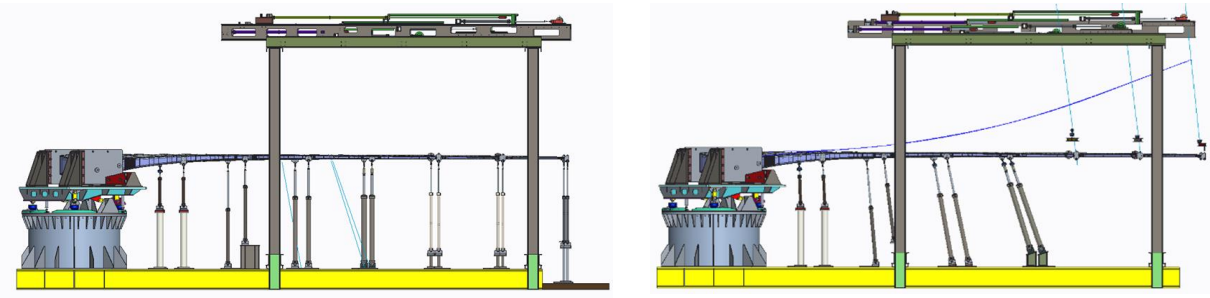

a) -1g and flexural axis b) 2.5g

Fig. 4: Test setups.

IV. Instrumentation

Instrumentation was installed on the PAT wing to measure both global and local responses of the wingbox, where global responses refer to displacements and rotations while local responses refer to strains. Figures 5 and 6 show photos of portions of the instrumentation setup from two different views.

To measure displacement, 17 string potentiometers were spatially distributed over the wingspan, attached to either the leading edge or the trailing edge spar webs. In addition, over 100 photogrammetry targets were distributed along the wing spars, as shown in Fig. 5. To measure rotations, 21 inclinometers were installed on the upper wing skin. Additional inclinometers were installed on the test fixture, to verify boundary rigidity, and also on the load lines to measure the load vector directions.

To measure strains, both conventional strain gauges and fiber optic strain sensors (FOSS) were installed on the wing. Each FOSS fiber had a strain grating sensor every 0.5 inches. A total of 412 conventional strain gauges, comprising axial gauges and rosettes, were applied to the wing. The majority of the gauges were installed on the tow-steered portions of the wing, with 143 gauges externally applied to the upper skin and 124 gauges externally applied to the lower wing skin. On seven rib bays of the upper skin, four axial strain gauges and three rosettes were installed internally to create back-to-back gauges for monitoring skin buckling. The remaining gauges were installed on the spars and ribs for analysis-to-test correlation. A total of eight FOSS fibers were applied in primarily spanwise directions on both the upper and lower skins. Each skin had a fiber located at the leading edge, midchord (at roughly the 40% chord), and trailing edge, as shown in Fig. 6. In addition, a "saw tooth" layout was used for the final fiber to create virtual FOSS rosettes (as shown in Fig. 6) to support research at NASA AFRC for calculating wing twist from skin strains. Since fasteners attached the skin to both the ribs and the spars, the FOSS needed to be carefully located on the wing to avoid the fasteners and their resulting stress concentrations. For example, in Fig. 6, the area circled in pink is where the fiber had to bypass a rib fastener. Additionally, as the diameter of the spar fasteners decreased in size (moving outboard), the fiber was routed closer to the respective leading and trailing edges, as shown by the yellow dashed line. Accelerometers, the instrumentation with the blue wires, are also visible in this photo and were used to support the ground vibration testing, but were not installed during static loads testing.

Finally, the speckle pattern on the upper skin used with LaRC's digital imaging correlation (DIC) system can be seen in Fig. 7. The speckle pattern extended a couple of ribs beyond the Yehudi break and loading station 2. The system's cameras were mounted on a boom and were able to detect the movement of the black dots and measure displacement fields, including local buckling, and calculate strains. Selected LaRC DIC results and how they were used for post-test correlation are presented in Ref. [10].

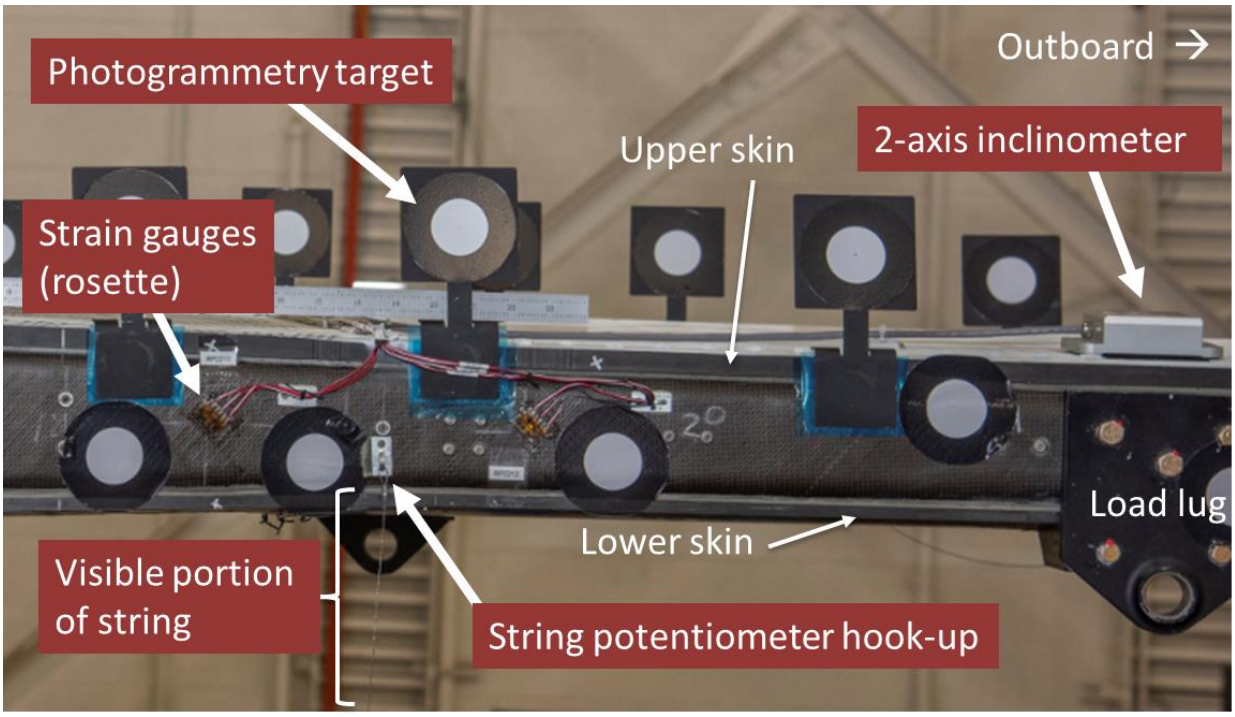

Fig. 5: View from rear. Photo of instrumentation on portion of trailing edge (at Yehudi break).

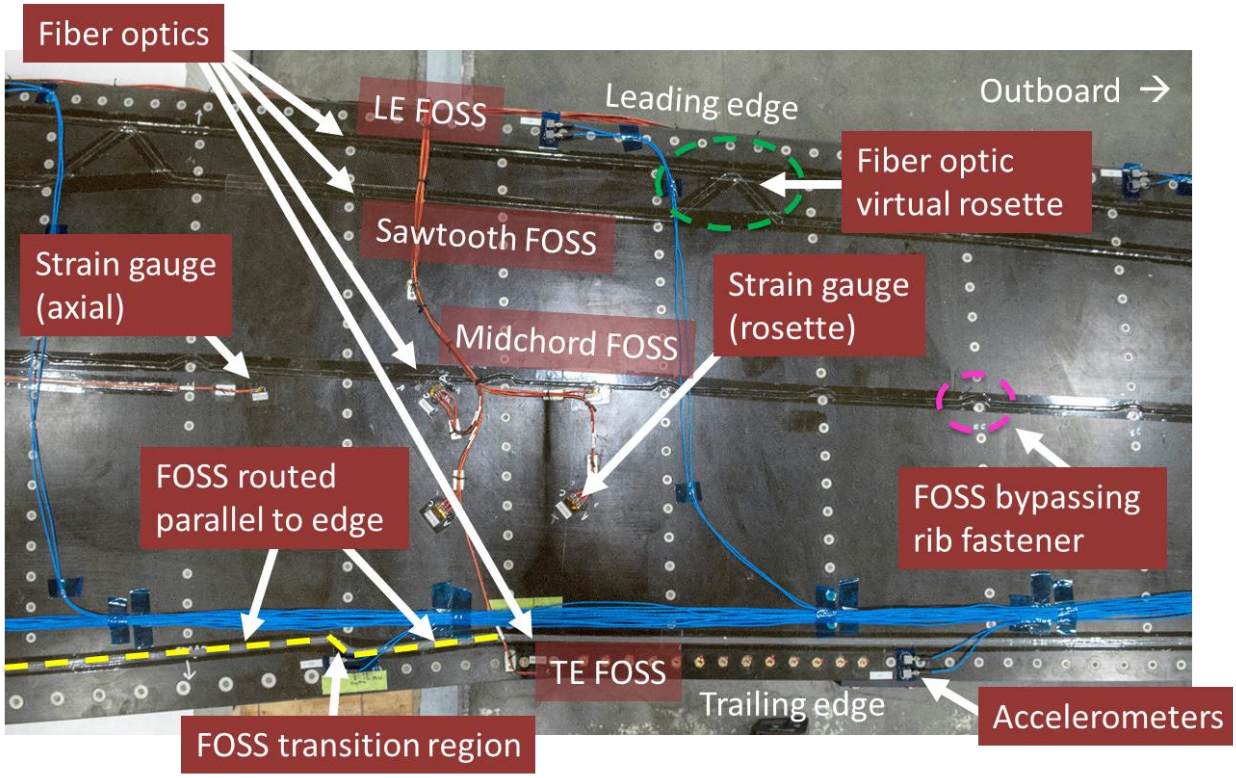

Fig. 6: View from above. Photo of instrumentation on portion of the upper skin (at Yehudi break).

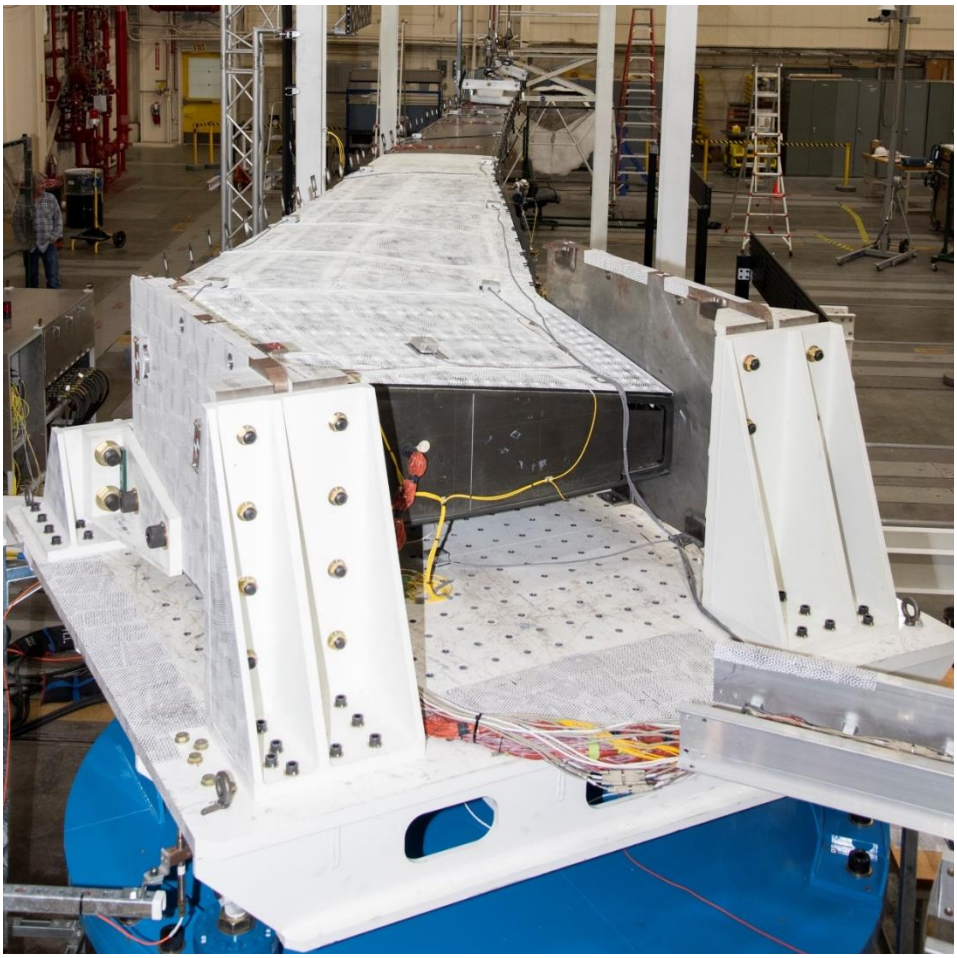

Fig. 7: The upper surface speckle pattern used for LaRC's digital imaging correlation.

V. Loading Sequence

Table 1 provides the largest load values applied during the individual tests. For the -1g and 2.5g maneuver tests, each load point was applied simultaneously to simulate a distributed load. These maneuver tests were each executed using a sequence of four loading cycles, with each cycle increasing in maximum load. The first loading cycle was scheduled for only 25% of the maximum load, shown in Table 1. The remaining three cycles were scheduled for 50%, 75%, and 100% of the maximum load, respectively. Before committing to the final load cycle, the sequence enabled technicians and engineers the opportunity to confirm successful test execution and make necessary adjustments, if needed. Engineers reviewed instrumentation outputs for both expected values and repeatability. Additionally, as the load increased within each cycle, the test was briefly paused at three periodic intervals, giving technicians and engineers additional opportunities to review the process.

To meet the objectives of the flexural axis test, point loads were individually applied to the wing at eight separate lugs, located at stations 4, 5, 6, and 7. Inboard of these load stations, the wingbox was relatively too stiff for the purpose of the flexural axis test. The applied loads were chosen to match the loads of the -1g test. For each load lug, the point load was cycled twice to 100% of the maximum load in Table 1. This process ensured repeatability of the test before moving to a new test point. For all loading scenarios, including the maneuver tests, the loads were applied slowly to represent static conditions.

Table 1: Applied loads (lb) per test.

Test	Location	Station 1	Station 2	Station 3	Station 4	Station 5	Station 6	Station 7
-1g maneuver	LE	-1906	-749	-1794	-1462	-1079	-592	-314
	TE	230	-604	622	694	726	401	235
Flexural axis	LE	na	na	na	-1462	-1079	-592	-314
	TE	na	na	na	694	726	401	235
2.5g maneuver	LE	3664	-1513	2777	2514	1417	937	219
	TE	2244	6674	1965	1323	1184	724	-69

VI. Results

This section summarizes the comparisons between the analysis and test results. MSC NASTRAN was used to determine the FEM predictions. As mentioned earlier, three types of static loads tests were performed on the wing: -1g maneuver test, flexural axis test, and 2.5g maneuver test. Figure 8 shows the maximum deflections for both of the simulated maneuver tests. The results from these tests will be covered first, with the flexural axis test to follow.

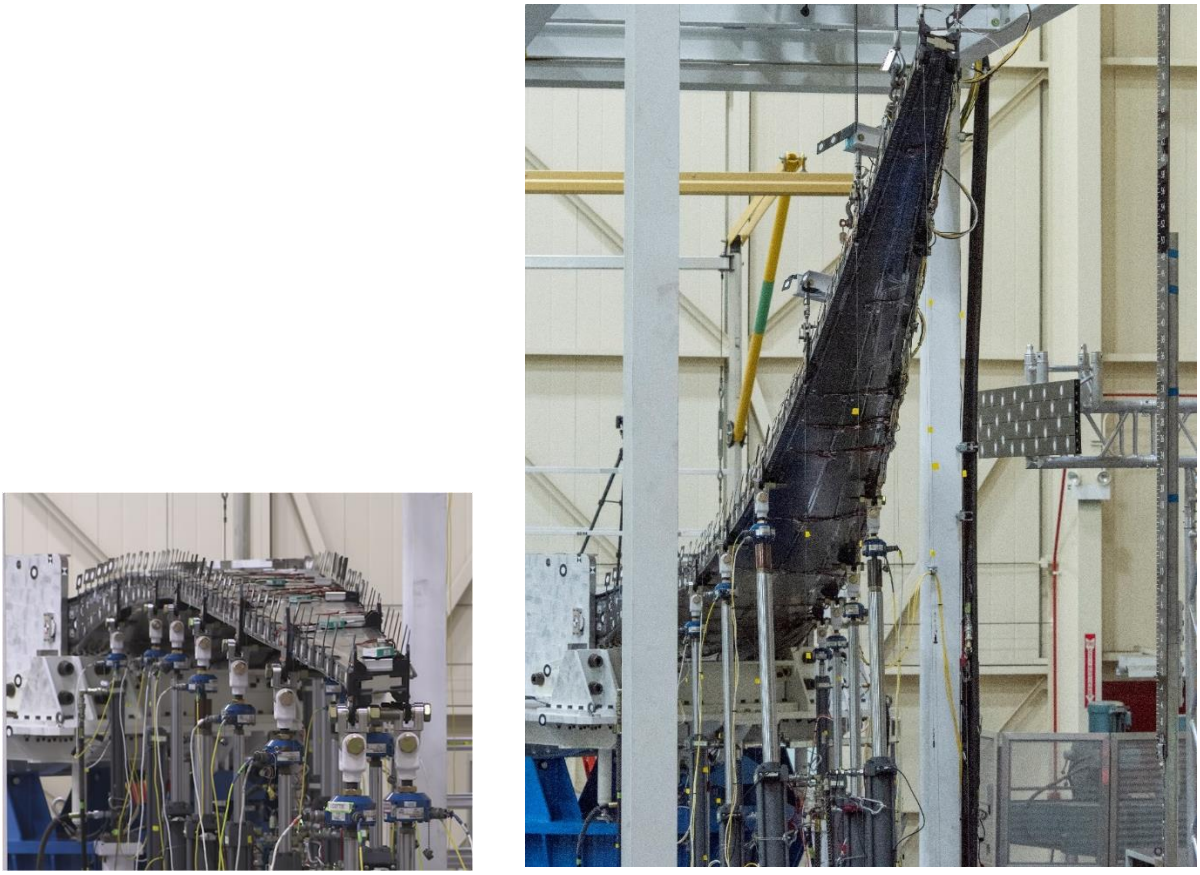

a) -1g load b) 2.5g load

Fig. 8: Maximum deflections of the two PAT wing maneuver tests.

A. Download (-1g) and Upload (2.5g) Maneuver Tests

The majority of the results presented in this section are from the 2.5g maneuver test, as this load condition had the greatest strain and deflection values. However, it should be noted that the maximum loads defined in Table 1 were not obtained for the 2.5g condition because as loads were being increased from the hold at 75% to 100% an event occurred that triggered an instability in the load control system near 90% of maximum load. Very large amplitude,

high-frequency loads were generated requiring an emergency load dump. However, in the process several locations were subjected to loads much larger than were planned to be applied, so no further testing was performed. Therefore, maximum load results for the 2.5g maneuver condition are presented herein at approximately 89.5% of the intended loads.

1. Global Response

Test data from string potentiometers, photogrammetry, and inclinometers were all used to measure the global response of the wing during the simulated maneuver loads. Figure 9 shows the displacement comparisons for the -1g and the 2.5g tests. The correlation of the test data with the model predictions match the bending and twist characteristics (trends) very well, but the displacements in tests were about 17% more than those expected from the model. For example, at the maximum 2.5g maneuver loads, the measured tip deflection was around 80 inches, while the predicted tip deflection was about 67 inches. Figure 10 provides the rotations and curvatures of the wing. The rotation measurements were taken from the inclinometers and rotated to a local coordinate frame that is parallel with the leading edge spar. The curvature values were calculated from these transformed inclinometer values. As with the displacements, the characteristics for bending and twist rotations are good, but as expected, the magnitudes exhibit poorer quantitative agreement. The curvature values at the wingtip show poorer correlation than the rotation measurements; however, this is partially due to the sensitivities encountered when taking a derivative from raw test data.

Many factors, unrelated to tow-steering, are likely to have affected the wing's global response. While the wingbox was being loaded and unloaded, engineers monitoring the test noticed small jumps (step functions) in the displacement data, especially near the boundary conditions at the wing root. Smith et. al. from Aurora Flight Sciences [6] examined the rotation data and projected 3.38 inches of displacement at the tip of the wing due purely to rigid body motion occurring at the wing root; this reduced the displacement discrepancies of the 2.5g loading condition from 17% to 13%. Lovejoy et. al. [10] from the NASA Langley Research Center post-processed the LaRC DIC data and the AFRC photogrammetry data. After adjusting for rigid body motion, the estimated displacement discrepancies fell within 4% on the inboard half of the wing and increased to about 12% at the wing tip.

Aurora notes in Ref. [6] that discrepancies between test and analysis are possibly due to the modeling of nonstructural features, such as the fastener stiffnesses and skin offsets. During fabrication of the test article, liquid shim was applied between the rib/spar skeleton and the upper and lower skins to minimize gaps in the construction, resulting in a thicker wing than designed. The FEM was subsequently updated to model the offsets within each skin; however, there was a level of uncertainty in the as-measured wing depth of the final test article. Therefore, it is possible that the offsets modeled in the FEM overcompensate for the actual increased wing depth. Further, although offsets were included in the FEM, the fasteners passing through the liquid shim were not updated for a potential lower stiffness due to increased thickness of the joints.

Although the global response of the wing shows discrepancies, the local response of the wing skin, which should be less affected by the modeling of nonstructural features and boundary conditions, exhibited good agreement between test and analysis, as is shown in the next section. In addition, the global response of the wing during the flexural axis test also compared well with the model. For these reasons, the reported FEM in this paper was not updated to provide the test and analysis correlation.

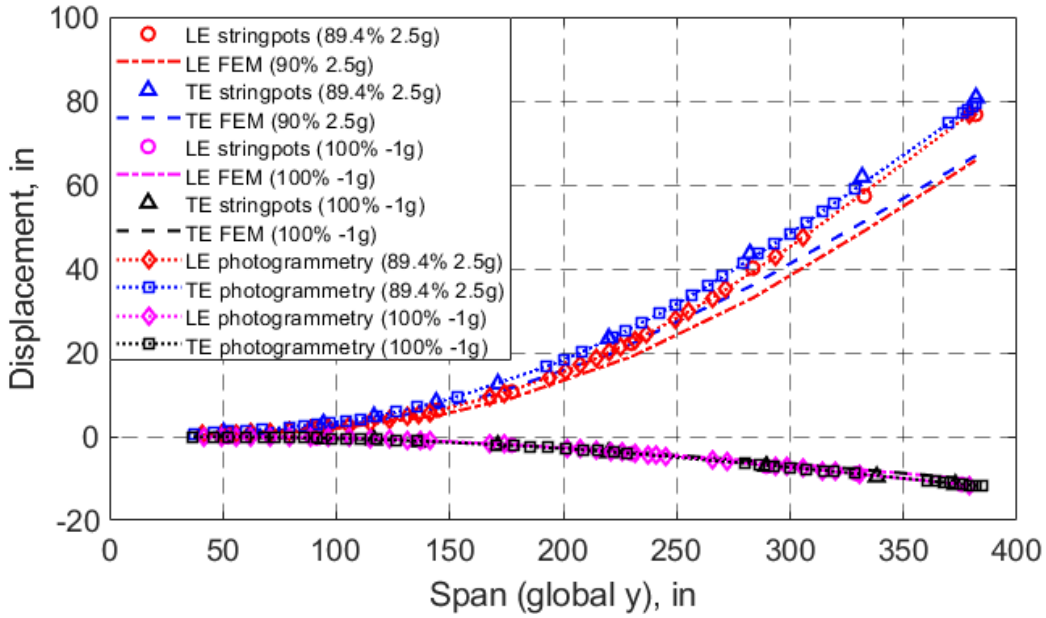

Fig. 9: Displacement values (magnitude) for the 2.5g and -1g load conditions. Magnitudes plotted in the direction of the wing vertical deflection.

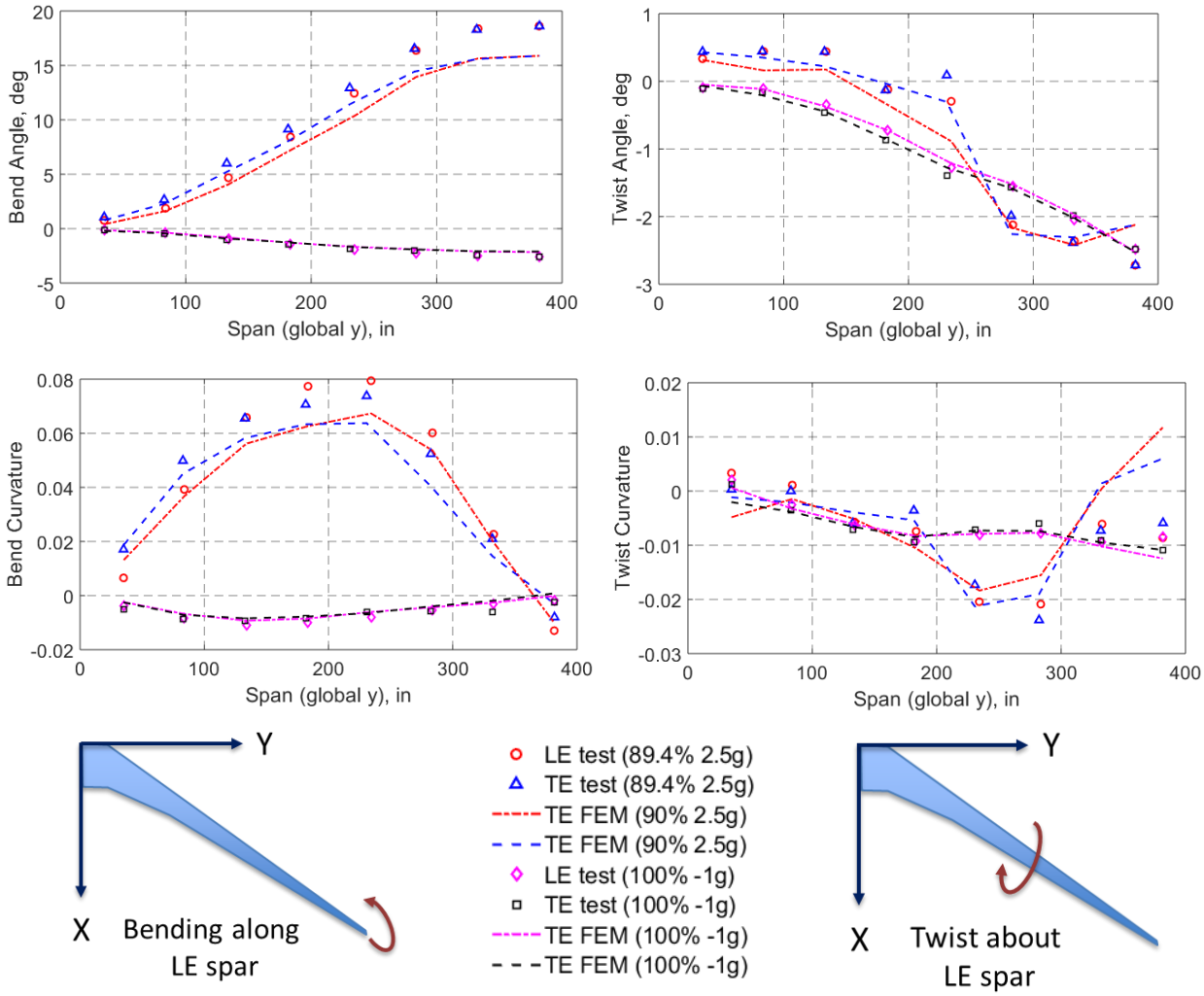

Fig. 10: Rotations and curvature values for the 2.5g and -1g load conditions.

2. Local Response

Unlike the global response of the wing that is highly sensitive to modeling inaccuracies that are unrelated to tow-steering, the local strain values are much less sensitive. During the simulated maneuver tests, the local response of the wing was measured using conventional strain gauges and FOSS. The majority of the strain measurements were taken on the tow-steered wing skins to support model validation.

Figures 11 - 13 show the strain values along the FOSS fibers located at the leading edge, midchord, and trailing edge, respectively, for both the upper and lower skin for the 2.5g maximum load condition. Each continuous FOSS fiber was routed using a series of line segments, with transition regions between the segments (as shown by the yellow dashed line in Fig. 6). Since the fiber had various orientations within the transition regions, strain data between two line segments were not used for comparison and appear as gaps in the FOSS and FEM data in the figures. The blue dotted lines represent the location of the ribs that intersect below the FOSS fiber. The pink dotted lines represent the locations of the seven load stations. Blue triangles indicate which strain values may be less accurate due to a local discontinuity in the fiber layout.

The test and nonlinear analysis results correlate well along the span of the wing. The lower skin shows better strain correlation between test and analysis than the upper skin, except at the very tip of the wing. However, Aurora

notes that the increased strain in the upper skin could be due to typical nonlinear reductions in a composite's material modulus when under compression [6]. These nonlinearities were not modeled in either skin's material system.

Certain areas of the FOSS fibers show spikes in the strain data. The spikes appear to coincide with the rib intersections, especially around midspan on the lower skin for both the leading edge and the midchord fibers. Being on the lower wing skin, the strains are primarily in tension. Furthermore, the leading edge and midchord locations have relatively larger wing depth (compared to the trailing edge) and more curvature (compared with the rest of the span). It is possible that the lower skin is not only in axial tension but also undergoing localized bending at the rib joints. The FEM does not model contact forces, which may explain why the predictions do not have these spikes.

On the upper skin, at 75 inches of span, analysis predicted nonlinear deformation across a few rib bays, which was most visible in the FEM results at the midchord. The FOSS and LaRC DIC data did not indicate the nonlinear response during the test. However, nonlinear deformation can be very sensitive to the as-built imperfections and local boundary conditions.

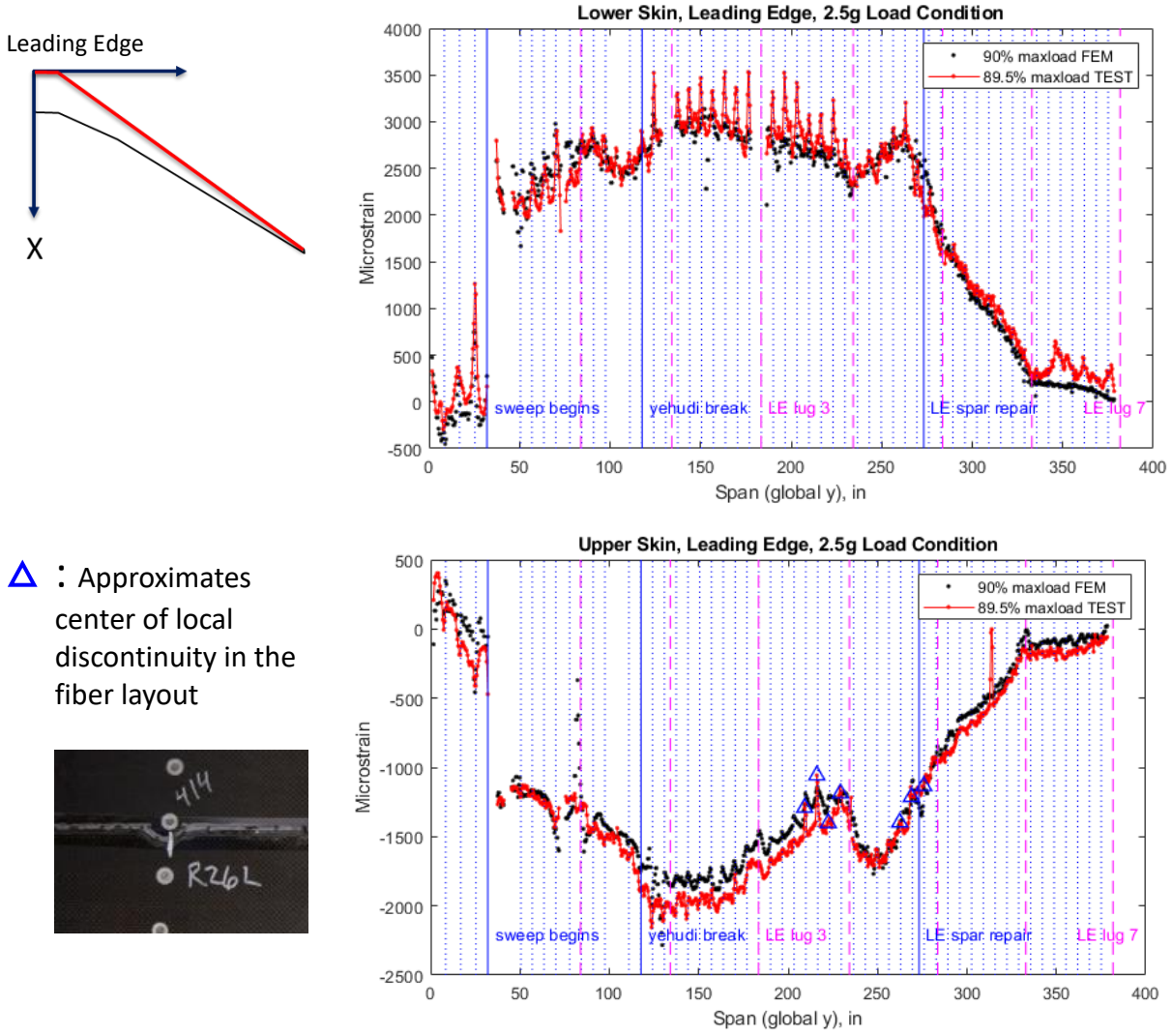

Fig. 11: FOSS values for the fibers on the leading edge for the 2.5g load condition. Dotted blue lines are locations of rib fasteners on the skin that intersect FOSS line segments. Pink dotted lines represent the location of the seven load stations.

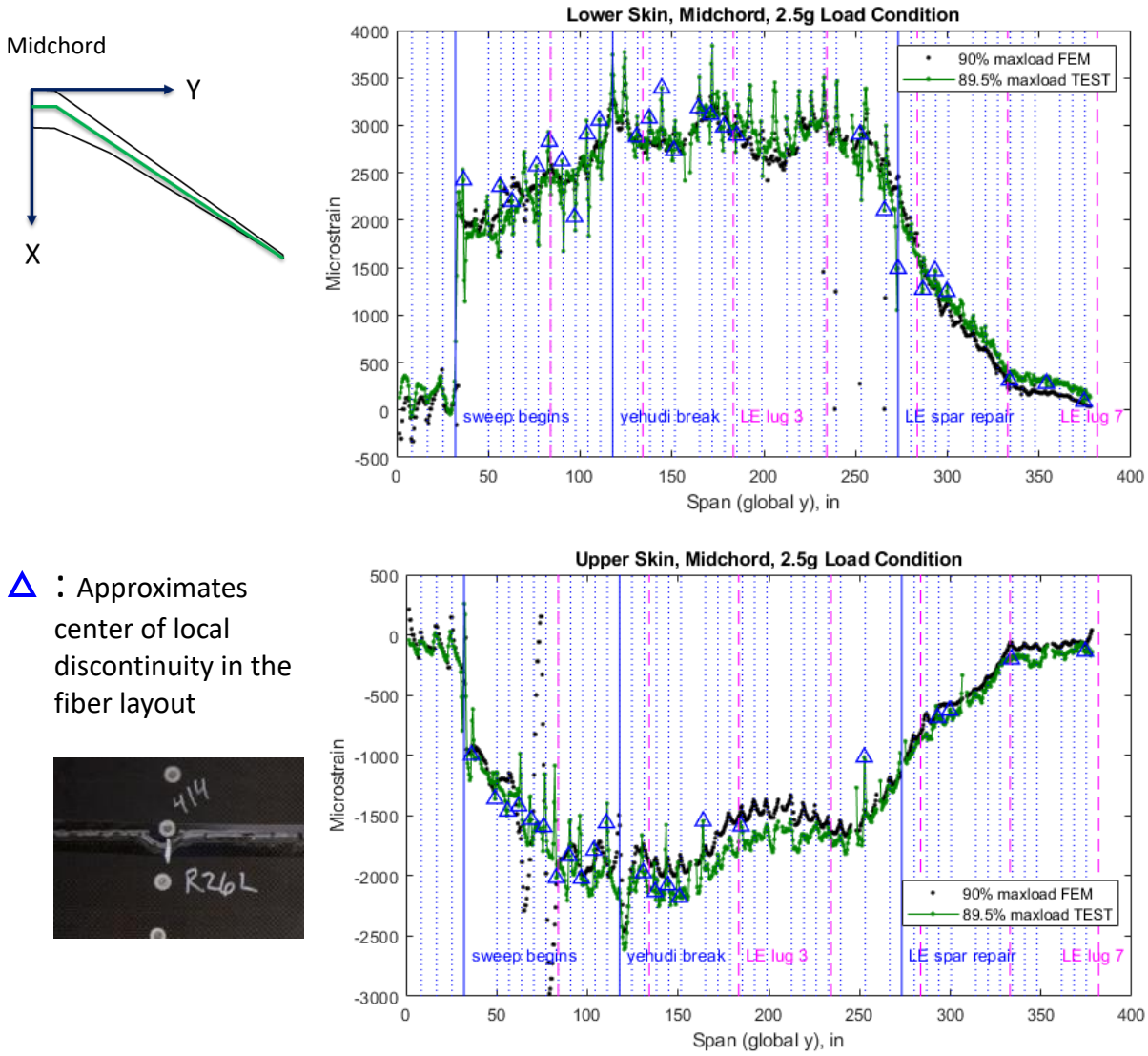

Fig. 12: FOSS values for the fibers on the midchord (near the 40% chord) for the 2.5g load condition. Dotted blue lines are locations of rib fasteners on the skin that intersect FOSS line segments. Pink dotted lines represent the location of the seven load stations.

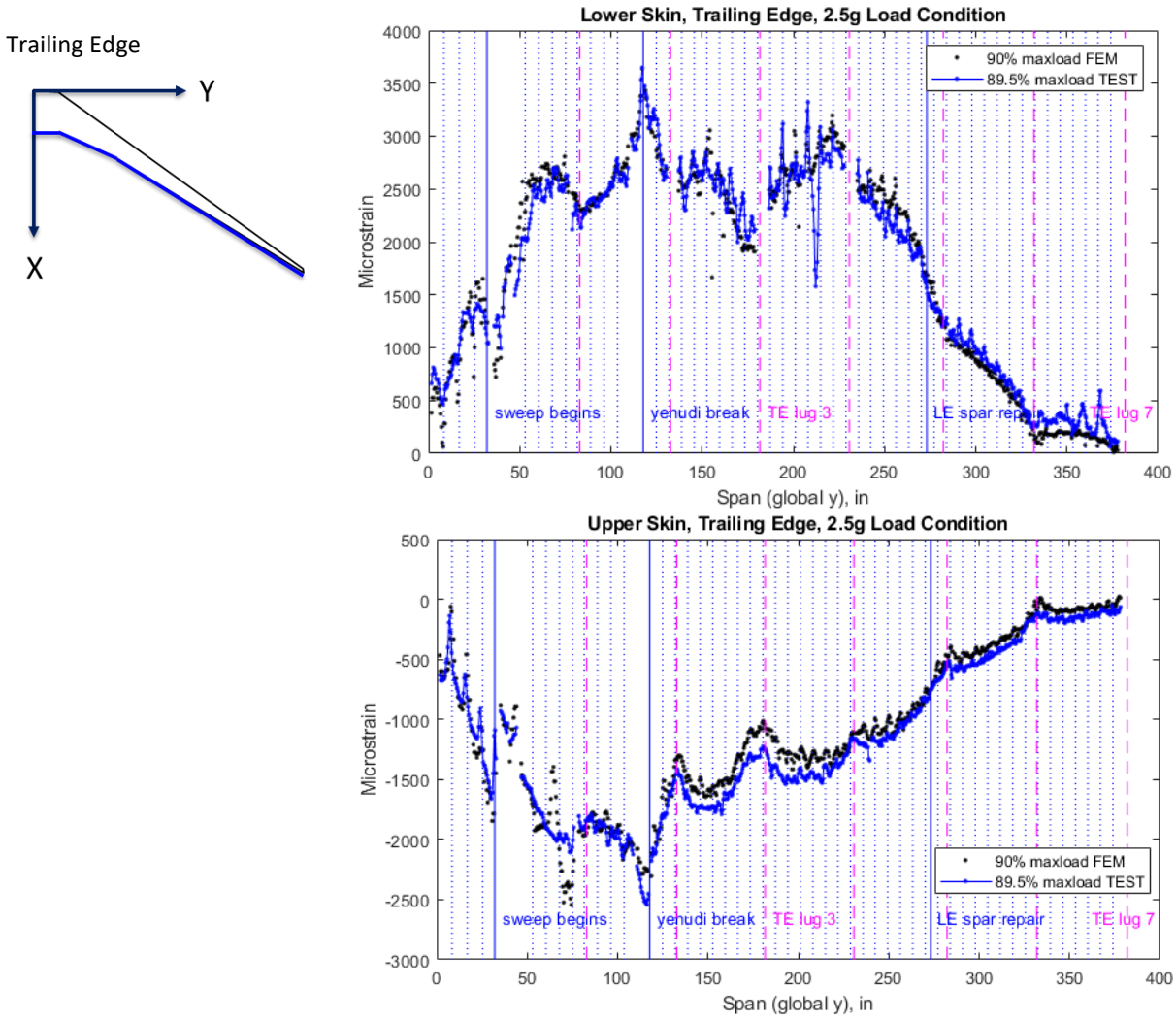

Fig. 13: FOSS values for the fibers on the trailing edge for the 2.5g load condition. Dotted blue lines are locations of rib fasteners on the skin that intersect FOSS line segments. Pink dotted lines represent the location of the seven load stations.

The FOSS results provide a high density of strain data along multiple one-dimensional paths. Because the composite fibers in the wing skins vary in their directionality throughout the wingspan, strain rosettes were arranged spatially over the upper and lower wing skins to capture strain responses within the planar surface of the skin. Wing sections with greater tow-steering curvature were targeted with a higher density of rosettes. Figure 14 shows rosette locations on both the upper and lower skins. As with the FOSS results, the rosettes are grouped by their general location: leading edge, midchord, and trailing edge. The plots in Fig. 15 show the corresponding FEM and test results for the principal strains. Since the upper skin was in compression and the lower skin was in tension, the plots show the min principal and max principal strains, respectively.

When reviewing the calculated principal strains and principal angles from the 79 rosettes installed on the wing skins, three rosettes appeared to have installation errors. When comparing their values to the model predictions, two channels of the three channels appeared to be switched for each of these rosettes. Applying the assumption that the channels were indeed switched, the resulting calculations of the principal strains and principal angles aligned with the predicted values. Additionally, two of the three rosettes were installed near measured FOSS strain virtual rosettes, which supported the channel switching hypothesis. Therefore, the updated data points are plotted with a "+" (rosette corrected), and the raw data points have an "x" through them (rosette incorrect). The third rosette of the three outliers was too far from any other sources of measured strain, making it difficult to verify switching of channels. Therefore,

the value of this third questionable rosette is plotted as calculated from the raw data and noted with an additional "□" (rosette questionable). Similar findings were provided in the post-processing of the strain data reported in Ref [6].

Skin strains are presented in Fig. 15, which shows the calculated principal strains generally match the model predictions. As seen in the FOSS results, the model predictions show varying strain values near the 75-inch span location on the upper skin's midchord region. Once again, the measured strains do not indicate that this nonlinear deformation occurred during test. Strains on the lower skin near the wing's root, approximately the 4 inch span station, show relatively worse analysis-to-test correlation compared to the upper skin. However, this area is less relevant to the tow-steering correlation and it is a difficult area to model, since the wingbox's boundary conditions are outboard of this location.

Knowing the magnitude of the principal strains compared well, it was important to also confirm the direction of the strains, especially since the underlying fibers within the skin vary their direction throughout the wing skins. Figure 16 shows plots of the principal strain orientations. The upper skin data uses the principal strain angle corresponding to the minor (min) principal axis, while the lower skin data uses the principal angles corresponding to the major (max) principal axis. Except for the aforementioned outlier whose outputs from the rosette are questionable as noted with an additional "□", the principal angles match closely with the model predictions. Since this test article is unique in its tow-steered wing skin construction, these results provide additional validation of the modeling technique employed for tow steering.

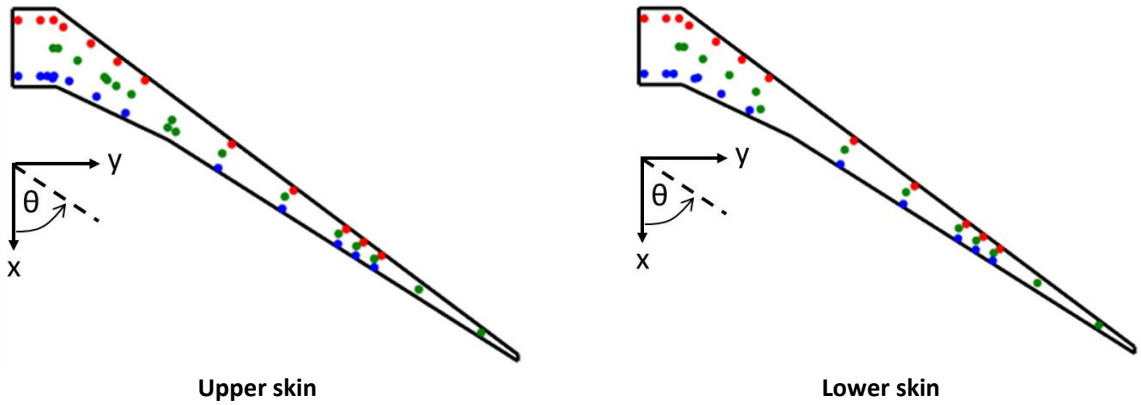

Fig. 14: Location of external rosettes on the upper and lower skins: leading edge (red), midchord (green), and trailing edge (blue).

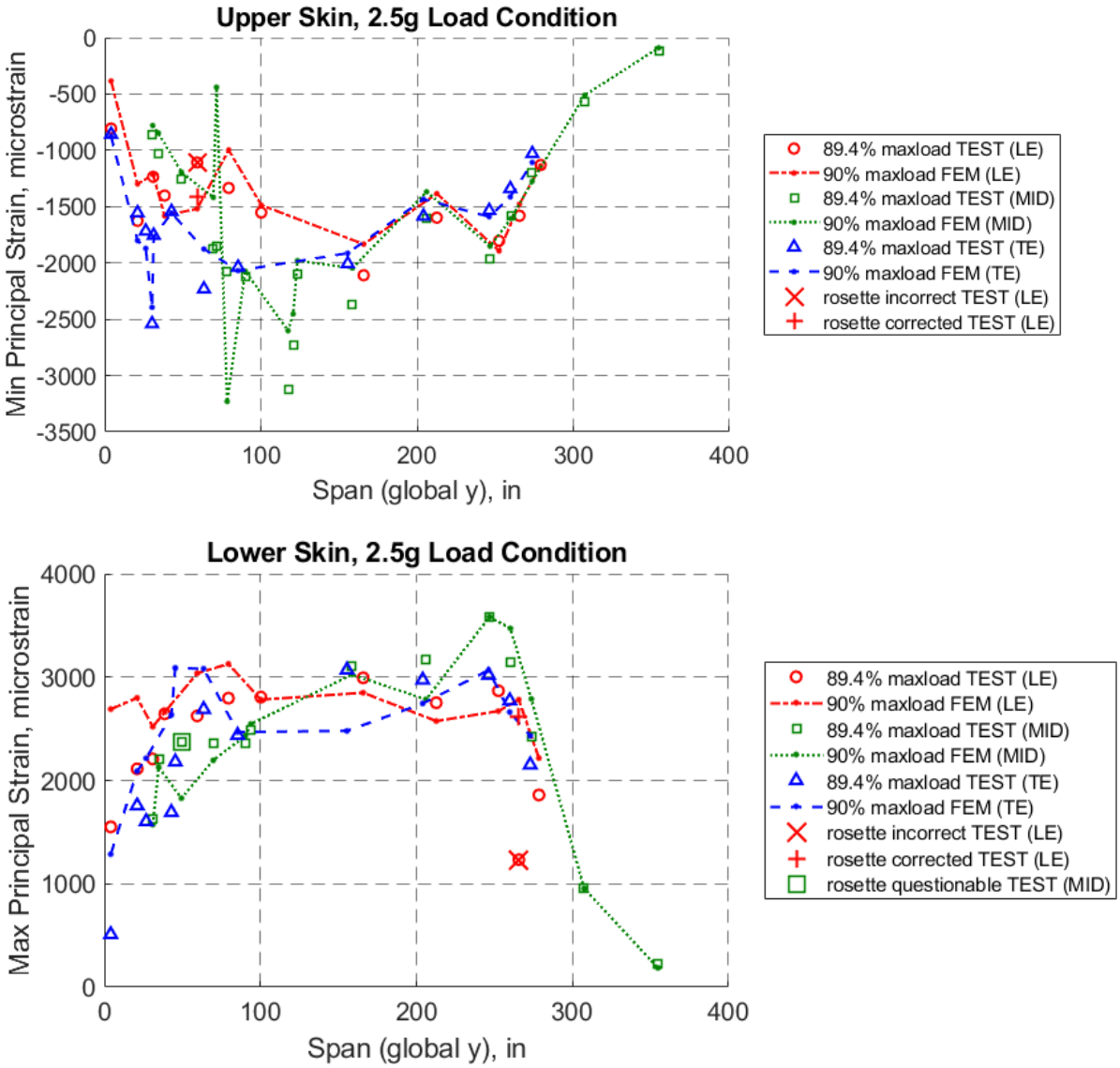

Fig. 15: Principal strain values for the 2.5g load condition. Min principal strain values are shown on the upper skin since it is in compression. Max principal strain values are shown on the lower skin since it is in tension.

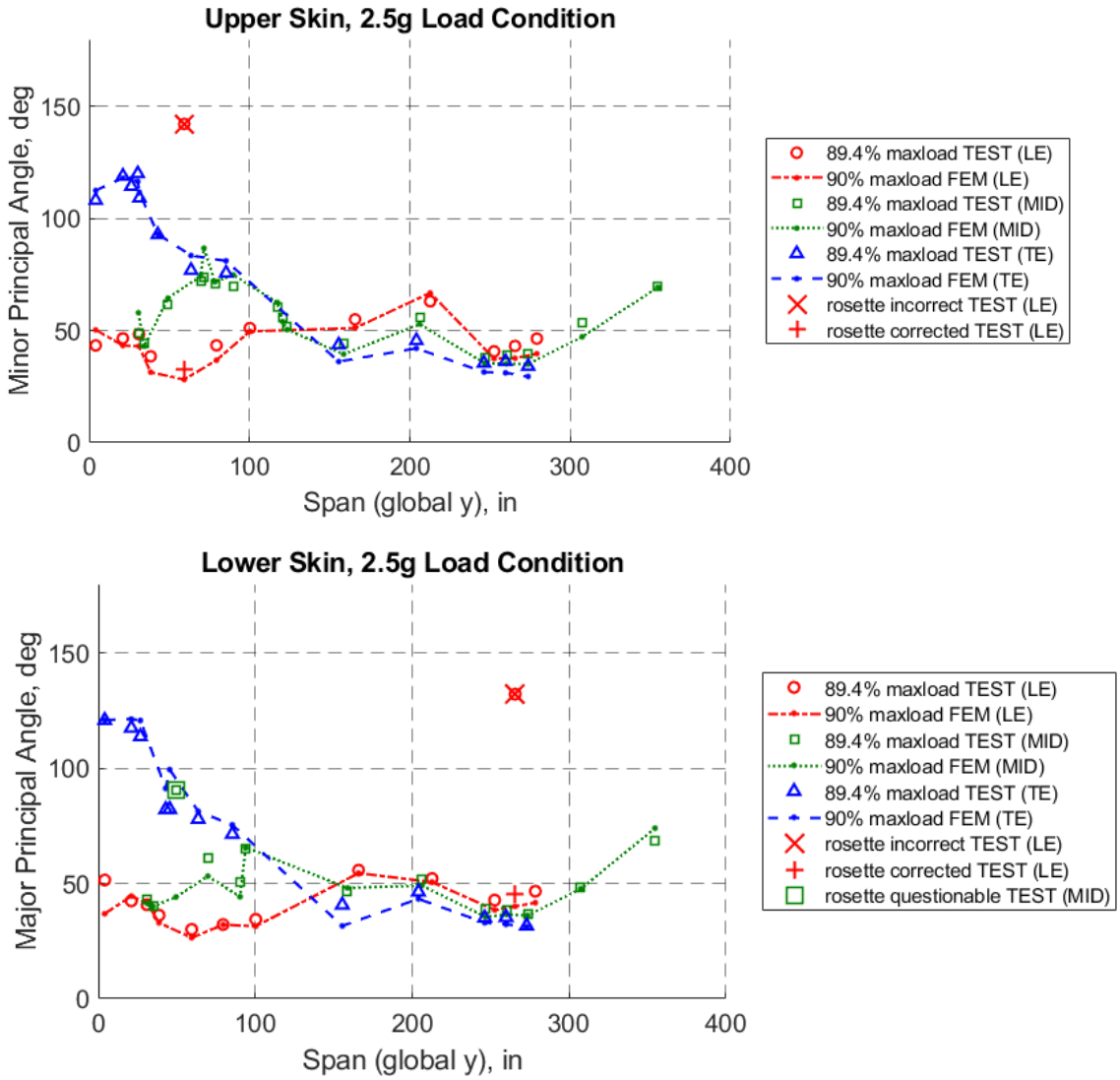

Fig. 16: Principal strain angles for the 2.5g load condition. Minor principal angles are shown on the upper skin since it is in compression. Major principal angles are shown on the lower skin since it is in tension.

B. Flexural Axis Test

The flexural axis of a wing is a locus of points that if concentrated loads were applied there, the resulting bending and twist response of the wing would not alter the angle of attack [11]. The purpose of the flexural axis testing was to characterize the bend-twist coupling response of the wingbox and compare it to the model prediction. This is especially relevant to tow-steered structures, since a composite structure's bend-twist coupling properties can be modified using tow-steering. Since the wingbox was optimized for vehicle fuel efficiency, it is important that the bend-twist response of the wing be preserved from model to build.

For the test, the wingbox's flexural axis was measured at four load stations along the wing that were located at the 4^{th}, 5^{th}, 6^{th}, and 7^{th} load stations. Four 2-axis inclinometers were designated specifically for the flexural axis test. Each inclinometer was located at the midchord of the wingbox, and its local X-axis was oriented along the line connecting the leading edge and trailing edge load lugs. The remaining axis, the Y-axis, measured the local twist.

The data required for the flexural axis test were acquired in the following manner. At a single span station, a point load was first applied to the leading edge lug, and then unloaded. To ensure repeatability, the load was cycled a second time. Next, a point load was applied to the trailing edge and also cycled twice. During these loading cycles, the

rotations of the wingbox were recorded by all the inclinometers on the wing, in addition to those designated for the flexural axis test.

At a single load station, it is ideal for the pairs of leading and trailing edge load lugs to be located at the exact same span location, i.e., the same global Y coordinate. However, due to manufacturing constraints, the lines connecting the leading and trailing edge load lugs were not perfectly aligned with the global axis, but the lines were within 10 degrees of the ideal alignment. Since the FEM had the same alignments as the test article, the calculations of the local flexural axis points were still comparable between analysis and test.

Figure 17 and Eq. (1) show the formulation for calculating the location of the flexural axis at a single span station, where x is the location of the flexural axis with respect to the leading edge, L is the distance between the two loading points, F_1 and F_2 are the applied loads at the leading edge and trailing edge, respectively, and θ_1 and θ_2 are the resulting local twist rotations due to the leading edge and trailing edge loads, respectively. Equation 1 is a solution to a system of two linear equations, $y = Ax + B$, where y is the resulting normalized theta (e.g., θ_1 / F_1) and x is the location of the applied load with respect to the leading edge.

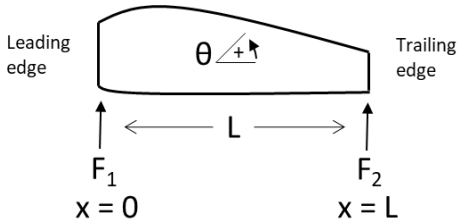

Fig. 17: Wingbox cross-section with definitions of the inputs to the flexural axis calculation.

$$x = \frac{\frac{\theta_1}{F_1} \times L}{\frac{\theta_1}{F_1} - \frac{\theta_2}{F_2}} \tag{1}$$

The results of the flexural axis test are shown in Fig. 18 and compared to the analysis. The figure legend shows that multiple opportunities were available to calculate flexural axis location, besides the originally planned tests using the hydraulic linear actuators and the midchord inclinometers, noted as "Hydraulic (MC inc)." The maneuver load tests included inclinometers at the leading edge, which were also recorded during the original flexural axis tests. These inclinometers had higher accuracy than the midchord inclinometers. Therefore, the rotations from the leading edge were first converted to align parallel with the midchord inclinometer and then used for the flexural axis calculation, i.e., "Hydraulic (LE inc)." In a separate study, after both the flexural axis test and the maneuver tests were completed, shot bags were hung from a beam that connected the pair of load lugs at each station. These shot bags were moved along several locations on the beam to determine the flexural axis location. Tests were repeated as needed, and the results are indicated in the legend as "Shot bags." Finally, before the test setup was disassembled, a series of "repeat" hydraulic tests were completed in February 2019 to check for repeatability, since the original flexural axis test had been conducted prior to the 2.5g maneuver load test and the shot bag tests.

Figure 18 shows that at each span station the results generally agree with the model prediction. Station 7 is located at the wing tip and has the most variability in its results. This may be explained by the relatively high compliance of this load station compared with the inboard stations, and secondly, the short distance between the leading and trailing edge lugs, L, magnifies any error in the force or rotation inputs to the equation. Aurora performed an independent calculation of the flexural axis and arrived at similar conclusions [6].

To provide more context to the flexural axis results, earlier in the PAT wing project, a trade study was performed using the PAT wing tow-steered configuration and additional unsteered (straight fiber) models that used the same laminate. When the fibers were straightened and oriented parallel to the leading edge, the flexural axis was located along the red line in Fig. 19. By rotating the straight fibers clockwise (CW) and counterclockwise (CCW) by 10 degrees, the location of the flexural axis shifts. Interestingly, the flexural axis of the -10 degree configuration is similar to the PAT Wing. This indicates that the two models may have a similar global response; however, the tow-steered design has additional benefits due to local tailoring of the composite. Local tailoring improves the stress and buckling response of the wing, enabling opportunities for weight reduction.

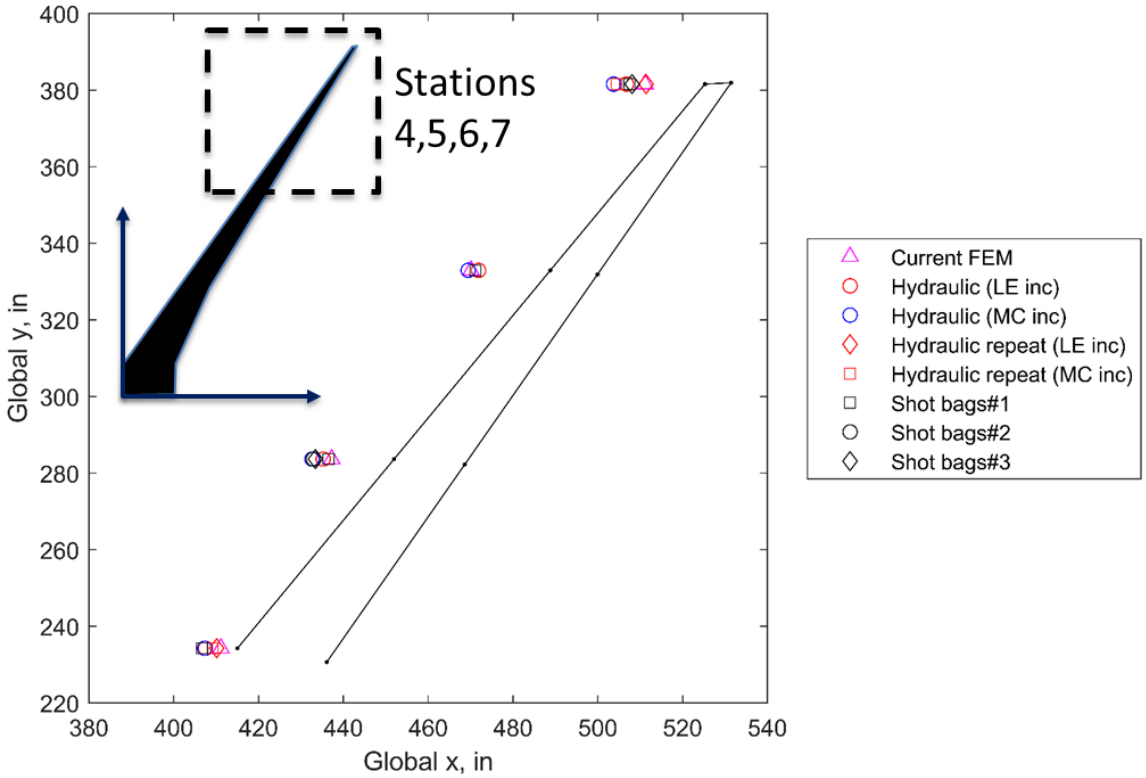

Fig. 18: Flexural axis results. The primary flexural axis test is noted as "Hydraulic (MC inc)" and "Hydraulic (LE inc)." The remaining data points were collected on later dates.

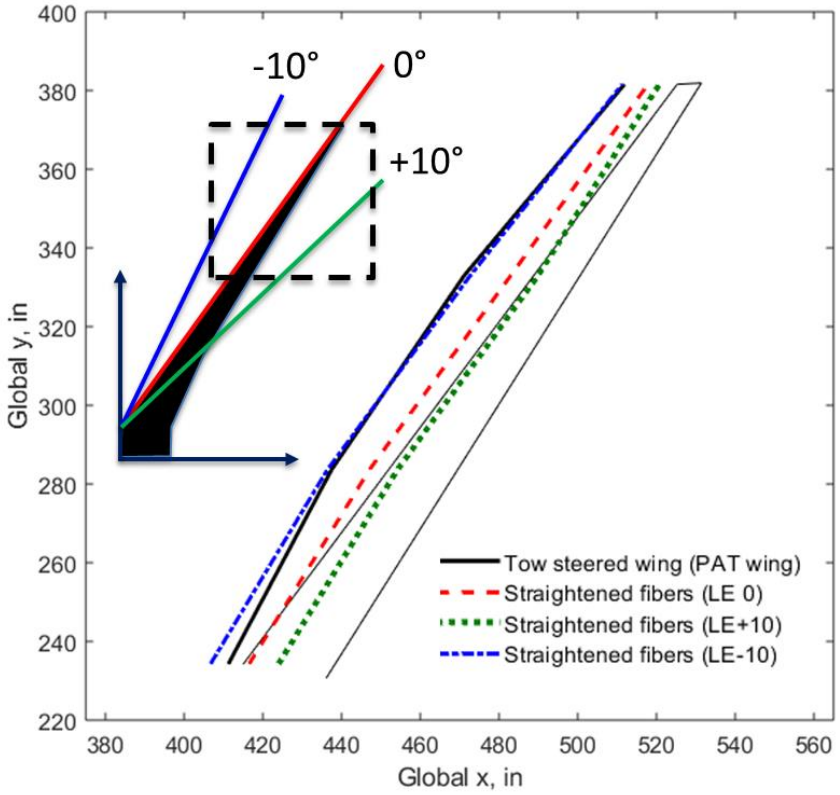

Fig. 19: Analytical results comparing the flexural axis location of the tow-steered PAT wing and three orientations of a straight fibered laminate.

VII. Conclusions

The objectives of the PAT wing static loads tests were successfully met during September and October 2018 in the NASA AFRC Flight Loads Lab. The test setup achieved sufficient loads to (i) characterize the wingbox response for simulated -1g and 2.5g maneuvers and (ii) determine the location of the wingbox's flexural axis. The instrumentation satisfactorily captured both local and global responses of the wing to enable desired model-to-test comparisons.

The results of the flexural axis test showed consistency with the model predictions. The global response of the wing (displacement and rotation measurements) under maneuver load conditions showed similar trends compared to the model predictions, though discrepancies of up to 17% were observed when comparing actual values between analysis and test. It was concluded that the boundary conditions and nonstructural features of the wingbox were the likely cause of the inconsistencies. The local response of the wingbox (strain measurements), which was much less sensitive to factors unrelated to tow-steering, exhibited good agreement with the predictions, validating the modelling techniques employed for tow-steered composites.

The PAT wing test article demonstrated the use of tow-steering at a scale large enough to employ fabrication methods similar to those used for full-scale structural fabrication. The results of the static loads tests were consistent with the conclusions of the PAT wing ground vibration test [6-8], giving credibility to the benefits of tow-steering that have been quantified analytically for transport aircraft. In particular, the modeling techniques used to design and optimize the PAT wing considered in this work were used in Ref. [5] for optimization of full-scale wing structures. That work demonstrates reductions in wing weight and fuel burn directly obtained through tow-steering, as opposed to straight-fiber composites, or metallic wing structures.

Acknowledgments

This work is funded by the Advanced Air Transport Technology Project under the NASA Advanced Air Vehicles Program. Special thanks to Karen Taminger, Dawn Jegley, and Ray Grenoble at the NASA Langley Research Center; Larry Hudson, Natalie Spivey, Eric Miller, Frank Pena, Andrew Holguin, and the test support crew at the NASA Armstrong Flight Research Center; Ben Smith and Larry Wirsing at Aurora Flight Systems, and Quim Martins, Tim Brooks, Carlos Cesnik, and Christopher Lupp at the University of Michigan.

References

[1] Lukaszewicz, D.H.-J.A., Ward, C., Potter, K.D., "The Engineering Aspects of Automated Prepreg Layup: History, Present and Future," *Composites Part B: Engineering*, Vol. 43, No. 3, 2012, pp. 997–1009. doi: 10.1016/j.compositesb.2011.12.003

[2] Dodwell, T. J., Butler, R., Rhead, A.T., "Optimum Fiber Steering of Composite Plates for Buckling and Manufacturability," *AIAA Journal*, Vol. 54, No. 3, March 2016, pp. 1139-1142. doi: 10.2514/1.J054297

[3] Stanford, B.K., Jutte, C.V., "Comparison of Curvilinear Stiffeners and Tow Steered Composites for Aeroelastic Tailoring of Aircraft Wings," *Computers and Structures*, Vol. 183, 2017, pp. 48-60. doi: 10.1016/j.compstruc.2017.01.010

[4] Stodieck, O., Couper, J.E., Weaver, P.M., Kealy, P., "Aeroelastic Tailoring of a Representative Wing Box Using Tow-Steered Composites," *AIAA Journal*, Vol. 55, No. 4, April 2017, pp. 1425-1439. doi: 10.2514/1.J055364

[5] Brooks, T.R., Martins, J.R.R.A., Kennedy, G.J., "High-fidelity aerostructural optimization of tow-steered composite wings," *Journal of Fluids and Structures*, Vol. 88, July 2019, pp. 122-147. doi: 10.1016/j.jfluidstructs.2019.04.005

[6] Smith, B., Brooks, T. Leader, M., Chin, T.W., Kennedy, G., Martins, J., and Cesnik, C., "Passive Aeroelastic Tailoring Final Report," NASA CR in preparation.

[7] Spivey, Natalie, "Ground Vibration Testing at NASA Armstrong Emphasizing on Passive Aeroelastic Tailored Wing Ground Vibration Test using Fixed Base Correction Method," *British Society for Strain Measurement (BSSM) 14th International Conference on Advances in Experimental Mechanics* in Belfast, Northern Ireland, United Kingdom, September 10 – 12, 2019.

[8] Spivey, N., Saltzman, R., Wieseman, C., Napolitano, K., Smith, B., "Passive Aeroelastic Tailored Wing Modal Test Using the Fixed Base Correction Method," *Proceedings of the IMAC-XXXVIII*, 2020. (To be presented.)

[9] Brooks, T.R., Kenway, G.K.W., Martins, J.R.R.A., "Benchmark Aerostructural Models for the Study of Transonic Aircraft Wings," *AIAA Journal*, Vol. 56, No. 7, July 2018, pp. 2840-2855. doi: 10.2514/1.J056603

[10] Lovejoy, A. E., Garndner, N. W., Dawicke, D. S., Jutte, C. V., and Smith, B., "Improving Structural Test and Analysis Correlation Using Digital Image Correlation Boundary Measurements," AIAA paper to be presented, *AIAA SciTech Forum*, Orlando, FL, January 6-10, 2020.

[11] Weisshaar, T., Nam, C., Batista-Rodriguez, A., "Aeroelastic Tailoring for Improved UAV Performance," *AIAA Structures, Structural Dynamics, and Materials Conference*, Long Beach, CA, April 20-23, 1998. doi: 10.2514/6.1998-1757